# Medium Voltage AC to Isolated Multi-port DC Converter for Electric Vehicle Fast-charging Stations

Harisyam P V, *Student Member, IEEE,* Saichand Kasicheyanula, Surjakanta Mazumder, *Student Member, IEEE,* Shashidhar Mathapati, Kaushik Basu, *Senior Member, IEEE,*

***Abstract*—The DC fast charging stations operate at megawatt-scale power levels, drawing energy from the medium voltage AC (MVAC) grid to reduce transmission losses. It also requires local energy storage and the capability for renewable integration to reduce the load on the grid. Conventional solutions use a bulky line frequency transformer (LFT) to step down MVAC to low voltage AC (LVAC), followed by multiple AC-DC and isolated DC-DC converters, leading to lower efficiency especially during power flow between local storage and electric vehicles. Existing multiport MVAC-to-LVDC converters often rely on modular multilevel converters (MMC), which has higher component count, or cascaded H-bridge (CHB) solutions with additional battery storage and additional bridges for power exchange. This paper proposes a novel CHB-based multi-port topology that eliminates the need for additional battery storage, additional semiconductor devices, and additional MV-insulated transformer winding compared to an MVAC to single port LVDC converter. The proposed modulation and control strategy ensures the independent operation of each LVDC port, and unity power factor operation at the grid interface. A step-by-step design for an 11 kV two-port converter is presented, and experimental validation is performed using a 1.2 kW laboratory-scale prototype with an efficiency of 95.3% at rated load.**

***Index Terms*—Medium Voltage, MVAC, Fast charging, Multi-port, Solid State Transformer, Bidirectional, Electric Vehicle**

## NOMENCLATURE

| | |
|---|---|
| MVAC | Medium voltage AC |
| LVAC | Low voltage AC |
| LVDC | Low voltage DC |
| VA | Volt Ampere |
| ISOP | Input series output parallel |
| SST | Solid state transformer |
| LFT | Line frequency transformer |
| HFT | High frequency transformer |
| MTx | Main transformer |
| IMTx | Inter module transformer |
| SPS | Single phase shift |
| CHB | Cascaded H-bridge |
| MMC | Modular multi-level converter |
| $r$ | No. of modules connected in series |
| $m$ | No. of load ports |
| $f_s$ | DC-DC stage switching frequency |
| $T_s$ | Switching cycle period $(1/f_s)$ |
| $f$ | Grid frequency |
| $V_{dc}$ | Floating DC link voltage |
| $v_g$ | Grid voltage |
| $\delta$ | Phase shift between DAB bridges |
| $r_j$ | No. of modules combined for $j^{th}$ port |
| $L_j$ | Series inductance for the IMTx for port $j$ |
| $P_j$ | Power flowing out of port $j$ |
| $\delta_{jj}$ | Phase shift between AC side bridge and DC side bridge for the $j^{th}$ port |
| $V_j$ | DC voltage for the port $j$ |
| $P_{IMTj}$ | Net power from port $j$ to IMTx. |
| $I_j$ | Current flowing to the port j. |
| $P_j(s)$ | Dynamic model of load for port $j$ |
| $C_j(s)$ | Voltage controller for port $j$ |
| $P_c$ | Power flowing through the MTx |
| $1:n$ | MTx turns ratio |
| $L_{MT}$ | Series inductance for the MTx |
| $\delta_{ij}$ | Phase shift between DC side bridges of port $i$ and port $j$ |
| $L_{ij}$ | Equivalent inductance between port $i$ and $j$ through IMTx |
| $P_{ij}$ | Power flow between port $i$ and $j$ through IMTx. |

An earlier version of this paper was presented in part at the 2023 IEEE Energy Conversion Congress and Exposition (ECCE) [DOI:10.1109/ECCE53617.2023.10362814 [1].

This work was supported in part by the Department of Science and Technology, Government of India under the project titled "Medium Voltage Grid Integration of Utility-Scale Renewable" through the Core Research Grant scheme.

## I. INTRODUCTION

THE demand for electric vehicle fast charging has increased due to advances in battery technology, which reduce charging time. Currently, electric vehicle batteries are suitable for high-power charging in the 350 - 500 kW range, making the total cumulative power of grid-connected charging stations reach the megawatt range, [2], [3]. This level of power is drawn from a medium voltage (MV) grid at the primary distribution level to minimize transmission losses and improve system efficiency. Due to the high power demand and the absence of a well-defined temporal load profile at the charging station, ensuring grid stability is a challenge. Local battery

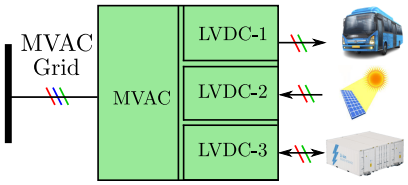


Fig. 1: A block diagram representation of upcoming MVAC to multi-port LVDC stations catering to various DC sources and loads with each isolated from one another.

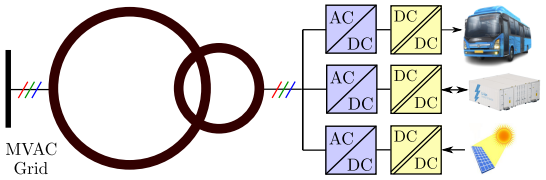


Fig. 2: Architecture of a line frequency transformer (LFT) based commercial EV fast charging stations.

storage is essential to have a smooth load curve independent of passenger arrival time to reduce the dynamic load on the grid. In order to reduce the dependency on fossil fuel-based grids and eliminate transmission loss, renewable energy sources can also be integrated into fast charging stations as shown in Fig. 1.

### A. *LFT-based and SST-based charging stations*

Modern electric vehicle fast charging stations must support more than 100 kW power per port increasing the system power rating [2]–[4]. Reference [4] discusses existing state-of-art DC fast chargers available in the market. Various charging protocols and charging systems, line frequency transformer (LFT) based AC/DC charger topologies, and SST based AC/DC module topologies are discussed in this article. LFT-based architecture, shown in Fig. 2, is the state-of-the-art commercial solution. The article also discusses topology configurations, existing products, prototypes developed for SST-based EV charging station. Different solid state transformers (SST) have been proposed in the literature to replace the combination of LFT and AC-DC with an MVAC to LVDC converter with a DC bus, [5]–[10]. SST-based solutions are a promising alternative to existing line frequency transformer based solutions due to the following reasons,

- SST-based solutions are compact, making it more suitable for DC urban charging stations, they have better power density, meaning more power available in the given real estate area [2]–[4], [11].
- Lower installation cost, with more than 40% cost reduction by elimination of bulky LV cables for high current and the corresponding switch-gear and transformer cost [2]–[4], [11].
- More efficient for AC-DC conversion with lower distribution losses on AC side [2]–[4], [11].
- SST-based solutions can be used for meeting ancillary requirements such as grid support, harmonic and reactive power compensation, grid firming, voltage and frequency support, [12], [13].

For a single port SST-based solution, isolated DC-DC converters are required to be connected to the DC bus to generate multiple isolated DC ports. Achieving high efficiency remains a key challenge in these solutions as the power still needs to flow through two DC-DC converters when energy transfers between two DC ports (for a cause of stored energy being used to charge a vehicle). This challenge can only be addressed by employing an MVAC to multi-port DC converter as shown in Fig. 1. Only a few topologies have been proposed

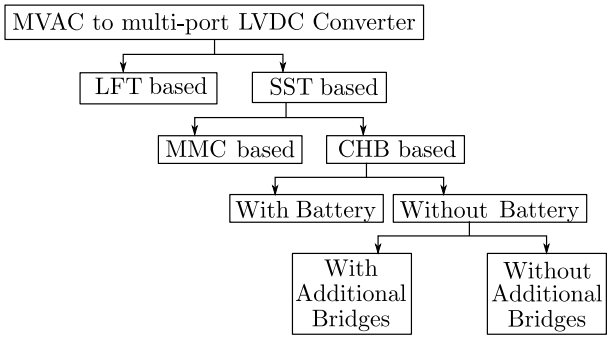


Fig. 3: Classification of MVAC to multi-port DC converters.

in the literature to generate multiple isolated DC ports from an MVAC grid where all ports are isolated with high-frequency transformers. A multi-port prototype with MV specifications and bidirectional power flow capability is yet to be developed.

### B. *MVAC to LVDC Converters with intermediate MVDC*

There is a class of MVAC to multi-port LVDC converters that first converts the MVAC to MVDC followed by MVDC to multi-port LVDC converter [14]–[18]. The first MVAC to MVDC stage is realized either with a modular multi-level converter (MMC) or with a two/three level AC-DC stage with medium voltage devices. Several MVDC to isolated multi-port LVDC architectures are proposed in the literature. Input series output parallel Triple-Active-Bridge (TAB) converters realize an MVDC to isolated multi-port LVDC converter in [15]. Dual-Active-Bridge DAB converters are series connected on the MVDC side, and a reactive (LC) branch is connected across two adjacent MVDC side bridges for power sharing in [16], [17]. An MMC-based half-bridge generates high-frequency MVAC from MVDC and passes through series-connected transformer primaries in [18]. The secondaries, followed by H-bridges, provide each isolated LVDC port. In [14], multiple isolated DC-DC and power-sharing converters are used to realize the MVDC to isolated multi-port LVDC converter. An NPC bridge is used to generate MVDC from MVAC with MV blocking devices. These medium voltage blocking devices are not commercially available and their switching causes high $dv/dt$ if the transient is not slowed down. Another possible approach to forming an intermediate MVDC bus from MVAC input is to use an MMC-based converter.

Converters with intermediate MVDC have the following disadvantages: 1) Solutions using NPC type of rectifier require MV blocking devices, which are not commercially available. Also, the switching needs to be slowed down to limit the $dv/dt$, resulting in higher switching loss. 2) MMC-based MVAC front-end rectifiers require twice the number of semiconductor devices when compared with CHB-based solutions. For example, the number of devices required to rectify an 11kV three-phase AC with devices that can form an 800V DC bus (1.2 kV device) for an MMC with half-bridge modules is 288 ( $\lceil 11\sqrt{2}/(0.8\sqrt{3})\rceil * 2 * 6 * 2$), whereas the number with a CHB full-bridge based solution is 144 ($\lceil 11\sqrt{2}/(0.8\sqrt{3})\rceil * 3 * 4$). The MMC-based solution requires

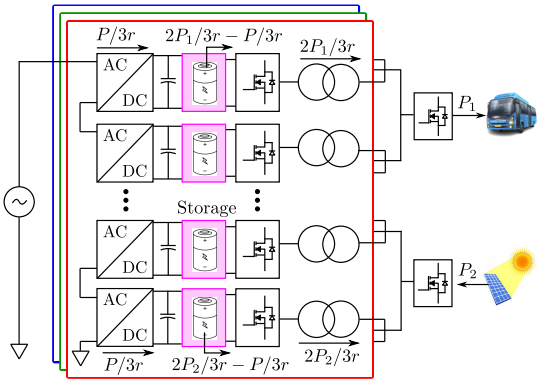


Fig. 4: MVAC to two-port topology in [20].

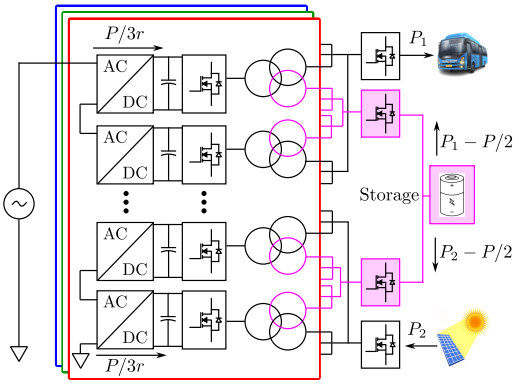


Fig. 5: MVAC to two-port topology in [21].

a higher number of module DC bus capacitors that also need to support fundamental frequency currents and, hence, lead to poor power density, [19].

### C. *CHB based solutions*

An alternative method involves initially converting MVAC to multiple floating LVDC buses using a cascaded H bridge (CHB) multi-level inverter, then derive low voltage DC ports from these floating DC buses. In [20]–[22] that are CHB-based, all the series connected modules of CHB carry the same current as they are connected in series. Since the series-connected modules also need to support medium voltage AC with low voltage devices, they generate nearly the same voltage to add up to medium voltage. This voltage generation is done through the control of CHB, requiring all modules to process the same amount of power, making it impossible to generate multiple ports from multiple modules. This challenge is overcome in [20] by proposing an interesting idea of generating multiple LVDC ports from each floating bus of CHB by accommodating battery storage in the intermediate DC link. Here, the two load ports require a power of $P_1$ and $P_2$, and the net power $P = P_1 + P_2$ is drawn from the grid. Considering a series connection of $r$ CHB modules per phase, each module processes a power of $P/3r$. The first port has a power requirement of $P_1$ from $3r/2$ modules combined after the high-frequency transformer (HFT). This indicates that each MV side bridge and the HFT process have a power of $2P_1/3r$ that is combined to form the first port. The difference in power for each module, $2P_1/3r - P/3r$, is supplied by battery in each intermediate DC link, as shown in Fig. 4. This allows all the CHB modules to process the same amount of power, as the battery can support different power for each port. The inclusion of numerous battery banks in intermediate floating DC links is an expensive solution that compromises long-term reliability (limited number of charge-discharge cycles) and power density.

The requirement of a battery bank in each floating DC link was modified with a single battery bank in [21]. This solution added an additional winding to each of the high-frequency transformers, and these windings (of a particular LVDC output port) are parallel connected to an h-bridge. The DC sides of all such H-bridges are connected in parallel and supported by a battery bank, as shown in Fig. 5. Assuming the two load ports are loaded with powers $P_1$ and $P_2$, net power drawn from the AC side is $P = P_1 + P_2$, and $r$ CHB modules are series-connected per phase, the power drawn by each CHB bridge is $P/3r$. Since the net load power for port 1 is $P_1$, the power supplied from the storage through the additional bridge to port 1 is $P_1 - P/2 = (P_1 - P_2)/2$. The power supplied from storage to port 2 is $P_2 - P/2 = (P_2 - P_1)/2$.

The use of a battery bank is eliminated in [22] by replacing the battery bank in [21] with a capacitor bank. This is feasible because the port does not require average DC power transfer ($P_1 - P/2 + P_2 - P/2 = P_1 + P_2 - P = 0$). However, [22] has the following disadvantages. 1) For each LVDC output port, an additional H-bridge is required. 2) The additional winding in each high-frequency transformer requires medium voltage isolation.

### D. *Comparison with CHB based solutions*

The proposed solution overcomes both of these limitations by introducing a multi-winding transformer that requires only low-voltage isolation. The proposed solution is compared with other CHB-based solutions, and this is summarized in the table. I.

An 11kV 400kW system is considered for comparison with two DC ports of 200kW each. The number of modules series connected per phase with 1200 V intermediate DC link is 12 to support 11kV MVAC grid. These intermediate DC bus voltages are controlled by the CHB stage and there is a requirement of 36 ($12 \times 3$) voltage sensors to measure each of these voltages. In addition to DC link voltages, it is also required to measure three phase voltages for the control of CHB stage. To control DC output voltages, there is also a requirement of two output voltage sensors, making the total count to 41 ($36 + 3 + 2$). For the solutions [21], [22] there is an additional port which also needs to be sensed, making the total count to 42 for these solutions. For the control of CHB stage there is a requirement to sense three phase current and for the control of output port, there is a requirement to sense the output current making to current sensor count to 5 ($3 + 2$) for the proposed solution and the solution proposed in [20]. However, for the solutions proposed in [21] and [22] this gets increased to 6 as the auxiliary port current also needs to be sensed.

TABLE I: Comparison of CHB-based MVAC to multi-port DC converters. 11kV grid voltage and two DC ports of 200 kW are considered for comparison. The number of devices on the CHB and AC side remains the same for all the solutions at 288.

| Reference | DC side Device count | Additional Battery bank | Semiconductor VA (per-unit) | Number of voltage sensor | Number of current sensor | No. of MV insulated HFT winding | Magnetic VA (per-unit) |
|---|---|---|---|---|---|---|---|
| [20] | 8 | Yes | 14.3 | 41 | 5 | 72 | 1.4 |
| [21] | 16 | Yes | 18.2 | 42 | 6 | 108 | 2.1 |
| [22] | 16 | No | 18.2 | 42 | 6 | 108 | 2.1 |
| **Proposed** | **8** | **No** | **14.3** | **41** | **5** | **72** | **2.1** |

The number of devices on the CHB stage and AC side bridge remains the same for all the solutions. Each AC-DC stage consists of 4 devices, with 12 modules connected in series per phase; the total number of devices in the CHB stage is 144 ($4 \times 12 \times 3$). Similarly, each AC side bridge is realized with four devices, making the total device count in the AC side bridge 144 ($4 \times 12 \times 3$). Each DC side bridge consists of 4 devices, and there is a bridge dedicated to each port. For the proposed solution and the solution proposed in [20], the DC side device count is 8. Solutions proposed in [21] and [22] there are two additional bridges required to connect to the auxiliary port, making the DC side device count 16. The maximum current through the device and the blocking voltage are the same for all the solutions.

There are 12 high-frequency transformers per phase that require medium voltage insulation, making the MV-insulated transformer count 36. The solution in [20] and the proposed solution have two-winding transformers, making the number of medium voltage insulated winding 72. However, the solutions proposed in [21] and [22] require a three-winding transformer, where the third winding is connected to the additional bridges feeding the auxiliary port. This makes the total MV insulated winding count 108. Per-unit magnetic VA is computed by calculating the sum of the product of RMS voltage across the transformer and the RMS current through the transformer.

### *E. Contribution of the paper*

A new MVAC to multi-port LVDC solution is proposed in this paper with the following advantages. It is compared to existing CHB-based multi-port solid state transformers, as given in Table. I. An experimental verification of the scaled down 1.2kW prototype is carried out with an efficiency of 95.3% at rated load.

- The topology is based on a CHB-based solution: a three-phase cascaded H-bridge inverter followed by multiple isolated DC-DC converters connected to the floating DC buses created by the multi-level inverter. The output high-frequency bridge of multiple DC-DC converters is combined with a single H-bridge to form one of the output DC ports. Similarly, all other DC output ports are formed. From this perspective, the proposed topology uses a similar architecture of the input series output parallel single DC port SST. No additional H-bridges are employed for multiple ports. ***So, the semiconductor VA of the proposed converter is the same as the single port ISOP SST architecture.*** The unbalance in power, when different ports are unequally loaded is addressed using a multi-winding transformer. ***This multi-winding transformer is realized at the LV side and, hence, is free of MV insulation.***
- A novel modulation strategy along with the feedback control architecture is proposed that ensures control of output port voltages, intermediate DC bus voltages, while drawing high-quality unity power factor (UPF) current from the MVAC grid.
- The proposed solution does not require additional battery storage and semiconductor devices compared to a MVAC to single port solution.
- A systematic design procedure for the proposed solution for an 11kV AC to 1000V two port system with a power rating of 400 kW is discussed.

The modulation, dynamic modelling, and control strategy of the proposed topology are discussed in the second section. A systematic design procedure with a medium voltage specification is discussed in the third section. This includes converter design, design of the inter-module transformer, and the DC side bridge design. Experimental results for a scaled-down prototype are given in the fourth section, and the fifth section concludes the paper.

## II. Analysis of the Converter

### *A. Topology Description*

The proposed converter architecture is shown in Fig. 6. A multi-level cascaded H-bridge (CHB) is connected to the MVAC side, with $r$ series connected H-bridges per phase. $r$ is decided by the blocking voltage of CHB devices and the peak of the line to neutral MVAC voltage. CHB is modulated with a well-known phase-shifted modulation strategy that results in power factor corrected balanced three-phase currents drawn from the MVAC port [23]. There are $m$ load ports; here, we assume $m < r$, which is the usual case. Load port $j$ is connected to $r_j$ H-bridges of the CHB in each phase through AC side bridges and high-frequency transformer, Fig. 6. $r_j$ is decided based on the rating of port $j$, satisfying the relation $\sum_{j=1}^{m} r_j = r$. A three-phase combination for port $j$ is done at the DC side after the high-frequency transformer and is connected to an H-bridge interfacing a load port. These transformers are termed as main transformer (MTx). So, for LVDC load $j$ port, there are $3r_j$ main transformers. Each H-bridge interfacing $m$ LVDC load port is connected to a $m$-

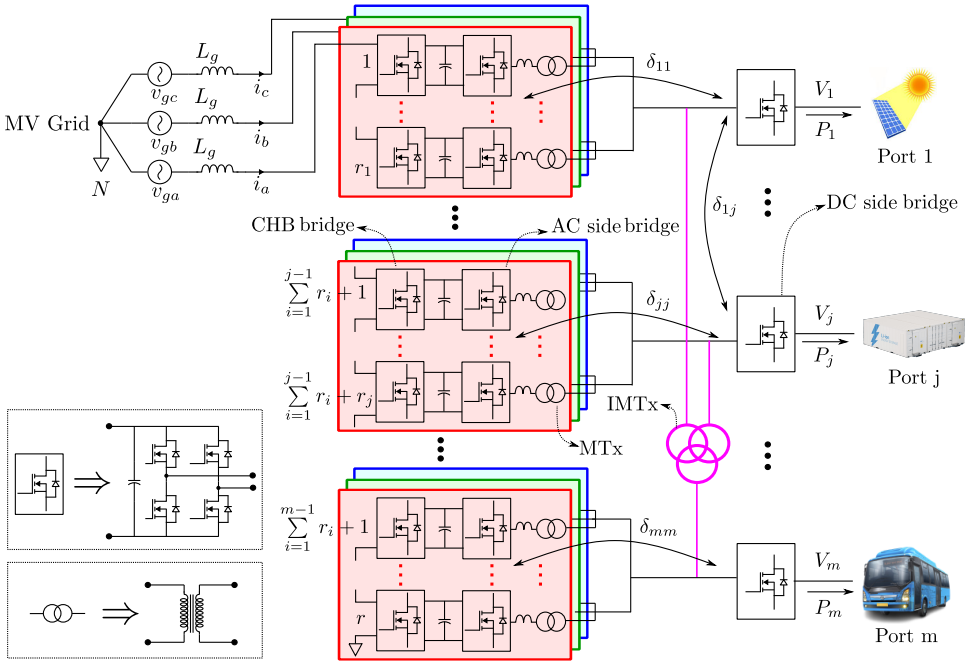


Fig. 6: Proposed Medium voltage AC to isolated multi-port converter with Inter Module Transformer (IMTx).

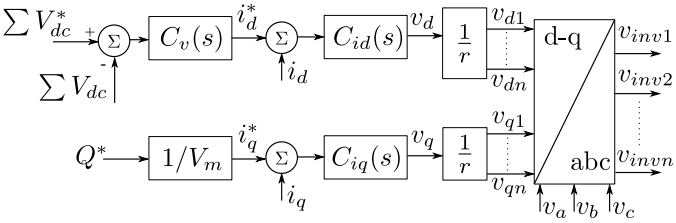


Fig. 7: Feedback control block diagram for the CHB stage.

winding transformer. This transformer is called inter-module-transformer (IMTx), enabling power transfer between ports.

### B. *Modulation strategy*

Phase shifted modulation strategy is adopted for the multi-level CHB to draw sinusoidal current from the grid. DC link voltage is regulated by the CHB to the required level in the grid following mode as discussed in [24], Fig. 7. The voltage loop generates the active power reference or d-axis component of the current, and the reactive power reference generates the q-axis component of the current. Voltage controllers generate the required d-axis component and q-axis component of voltage to track the respective current references. This voltage is transformed to an abc frame, followed by CHB modulation, to generate the required voltage on the grid side.

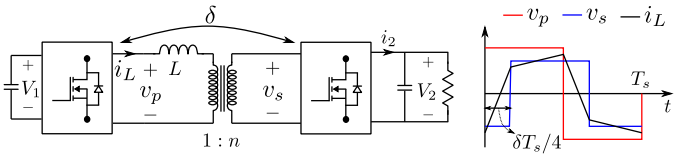


Fig. 8: Switching cycle waveform of a Dual Active Bridge.

The switching strategy for the rest of the high-frequency switched bridges indicated as AC side bridge and DC side bridge in Fig. 6 is discussed further. For simplicity, let us assume that there is no power loss in the converter. The dynamic model can be improved by incorporating the converter losses. However, this can lead to a complex operating point-dependent small signal model, which makes the control design challenging. The variation in the dynamic model incorporating the losses is minimal in the frequency region of interest, [25]. All H-bridges (AC side and DC side bridges) are modulated to generate a square wave of a given switching frequency ($f_s$) to transfer the required power to the DC side. The waveform for a DAB converter operated to generate square waveform (single phase shift (SPS) modulation) is given in Fig. 8. From the waveform, the power transferred from one port to the other is expressed as a function of voltages and converter parameters as given in (1).

$$P = \frac{V_1 V_2}{8 n f_s L} \delta (2 - |\delta|) \tag{1}$$

Incorporating the magnetizing and leakage inductance of the transformer can lead to a change in the power transfer inductor as shown (2) based on Fig. 9.

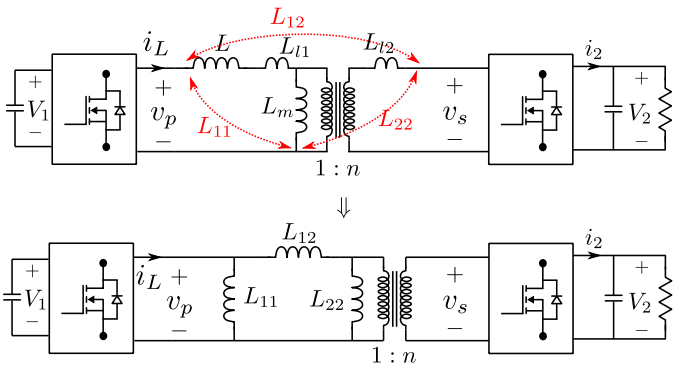


Fig. 9: Equivalent model of DAB with magnetizing inductance.

$$P = \frac{V_1 V_2}{8 n f_s L_{12}} \delta(2 - |\delta|) \tag{2}$$

$$L_{12} = \frac{n^2(L_{l1} + L)L_{l2} + (L_{l1} + L)L_m + n^2 L_m L_{l2}}{Lm} \tag{3}$$

This DAB operation is extended for the proposed multi-port converter. Power requirement in load port $j$ is $P_j$, and the net power requirement for all the load ports from the grid is $\Sigma P_j$, (5). CHB bridges and AC side H-bridges equally process this required power. All $3r$ AC side H bridges transfer the same amount of power $P_c$ given in (4).

$$P_c = \frac{1}{3r} \sum P_j \tag{4}$$

Considering the $j^{th}$ group, all $3r_j$ AC side H-bridges are identically modulated with a phase shift of $\delta_{jj}$ with respect to the square-wave generated by the DC side bridge connected to $j^{th}$ port. $L_{MT}$ is equivalent power tranfer inductance calculated based on (2). This includes the series inductance connected between each H-bridge and the main transformer, leakage inductance of the MTx and magnetizing inductance of MTx (there are a total of $3r_j$ of them in $j^{th}$ group). Extending (8) for the $j^{th}$ group, the power transferred through $3r_j$ main transformers as a function phase shift and converter parameters is given by (5). This can be represented as an equivalent DAB shown in Fig. 10.

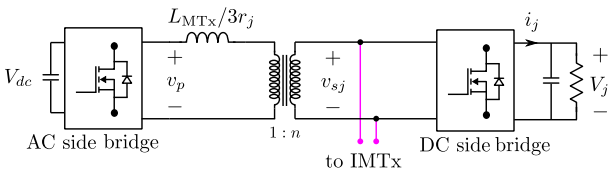


Fig. 10: Equivalent circuit to show power transfer through the main transformers (MTx) for the $j^{th}$ group leading to (5).

Since the power processed through each main transformer is the same, but the load requirement can be significantly different, there is power flow through the IMTx based on this difference. The phase shift between square waves generated by different DC side bridges determines the power transfer through the IMTx. The schematic for power flow through IMTx and the equivalent circuit are shown in Fig. 11. The multi winding IMTx has a turns ratio of 1:1 ... :1. From Fig. 11, the relation between power flow and phase shift is derived as (6). $V_i$ and $V_j$ are DC bus voltages of port $i$ and $j$ respectively. $\delta_{ij}$ is the phase shift between $i^{th}$ bridge and $j^{th}$ bridge at low voltage side. $L_{ij}$ is the equivalent inductance seen between ports $i$ and $j$ of the IMTx. The relation between $L_{ij}$ and the effective series inductors per winding, from Fig. 11, is given in (7).

$$3r_j P_c = \frac{3r_j V_{dc} V_j}{8 n f_s L_{MT}} \delta_{jj}(2 - |\delta_{jj}|) \tag{5}$$

$$P_{ij} = \frac{V_i V_j \delta_{ij}}{8 f_s L_{ij}} (2 - |\delta_{ij}|) \tag{6}$$

$$L_{ij} = L_i L_j \left( \frac{1}{L_1} + \frac{1}{L_2} + ... + \frac{1}{L_n} \right) \tag{7}$$

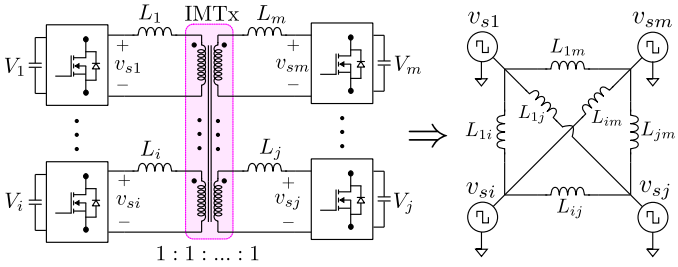


Fig. 11: Schematic of the IMTx and the equivalent circuit.

### C. *Dynamic model of the plant*

The switching cycle average current to the first port can be calculated by adding the component of power coming through the MTx and IMTx. From (5), the current from the component of power flow through the main transformer can be calculated as given in (8).

$$\frac{3r_1 P_c}{V_1} = \frac{3r_1 V_{dc}}{8 n f_s L_{MT}} \delta_{11}(2 - |\delta_{11}|) \tag{8}$$

The power flow in other groups also follows a similar relation with $\delta_{jj}$ and $V_j$ for the $j^{th}$ port. The current from the component of power flowing through the IMTx from the first port to the other ports is calculated as given in (9a) to (9e). These relations are added to calculate the power flowing to the first port through IMTx as given in (10a). This can be extended to calculate the power flowing to other ports as given in (10b) to (10f). There are only $m-1$ independent phase shifts between DC side bridges as $\delta_{12}, ...\delta_{1j}, ...\delta_{1m}$, and any other phase shift between the DC side bridges can be expressed as $\delta_{ij} = \delta_{1i} - \delta_{1j}$.

$$\frac{P_{12}}{V_1} = \frac{V_2}{8 f_s L_{12}} \delta_{12}(2 - |\delta_{12}|) \tag{9a}$$

$$... \tag{9b}$$

$$\frac{P_{1j}}{V_1} = \frac{V_j}{8 f_s L_{1j}} \delta_{1j}(2 - |\delta_{1j}|) \tag{9c}$$

$$... \tag{9d}$$

$$\frac{P_{1m}}{V_1} = \frac{V_m}{8 f_s L_{1m}} \delta_{1m}(2 - |\delta_{1m}|) \tag{9e}$$

$$P_{IMT1} = \sum_{j=2}^{m} P_{1j} = V_1 \sum_{j=2}^{m} \frac{V_j}{8 f_s L_{1j}} \delta_{1j}(2 - |\delta_{1j}|) \tag{10a}$$

$$P_{IMT2} = V_2 \sum_{\substack{j=1 \\ j \neq 2}}^{m} \frac{V_j}{8 f_s L_{2j}} \delta_{2j}(2 - |\delta_{2j}|) \tag{10b}$$

$$= V_2 \sum_{\substack{j=1 \\ j \neq 2}}^{m} \frac{V_j(\delta_{12} - \delta_{1j})(2 - |(\delta_{12} - \delta_{1j})|)}{8 f_s L_{2j}} \tag{10c}$$

$$... \tag{10d}$$

$$P_{IMTm} = V_m \sum_{j=2}^{m-1} \frac{V_j}{8 f_s L_{mj}} \delta_{mj}(2 - |\delta_{mj}|) \tag{10e}$$

$$= V_m \sum_{j=2}^{m-1} \frac{V_j(\delta_{1m} - \delta_{1j})(2 - |(\delta_{1m} - \delta_{1j})|)}{8 f_s L_{mj}} \tag{10f}$$

From (8) and (10f) the power flowing to the load port is $P_1 = 3r_1P_c - P_{IMT1}$, and the current supplied to port 1 is $I_1 = P_1/V_1$. The voltage of port 1 is decided based on the load current and the current flowing to the filter capacitor as shown in Fig. 12, and the model of IMTx is highlighted. The switching cycle average model of the converter is a static model except for the filter capacitor.

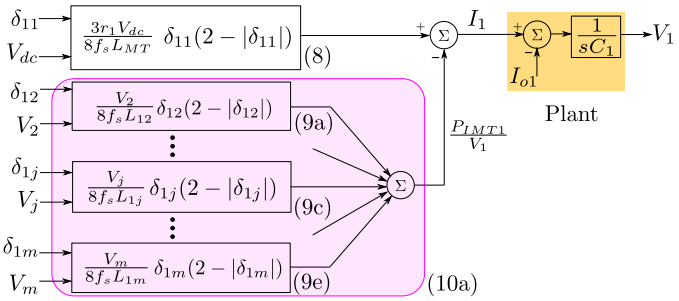


Fig. 12: Dynamic model of the plant for the port 1.

### D. *Control strategy*

The static nature of switching cycle average model of the converter from $\delta_{11}...\delta_{jj}..,\delta_{12}...\delta_{1j}...$ to $I_1...I_j...I_m$ is utilized to design the controller for the proposed converter. Load feed-forward is added to improve the transient response by eliminating the load dependency in transients. This also helps controller design for complex loads that are active in nature. The non-linear static model from phase shifts to current is inverted to simplify the voltage controller design for the plant from $I_j$ to $V_j$. This inversion simplifies the plant model from $I_j^*$ to $I_j$ as a unity gain block with an implementation delay including one switching cycle computation delay and half switching cycle delay for the switching cycle averaged model as given in (11). From (11), the loop gain, including the controller and the plant model, is given in (12), and controller $C_j(s)$ is designed with desired gain cross over frequency and phase margin, [26].

The calculation of phase shifts from the controller output is discussed further. The voltage controller for the $j^{th}$ port calculates the current reference $I_j^*$, which is multiplied by $V_j$ to get the required power demand. Power requirements in all the ports are added to get the total power demand and divided by $3r$ to calculate $P_c^*$. $\delta_{jj}$ is calculated from this $P_c^*$ for the $j^{th}$ group as given in (13) given $V_j$ and $V_{dc}$. This is shown in the block diagram Fig. 13.

$$I_j/I_j^* = 1e^{-3T_s/2} \tag{11}$$

$$L_j(s) = C_j(s) \cdot e^{-3T_s/2} \cdot \frac{1}{sC} \tag{12}$$

$$\delta_{jj} = f_j^{-1}(\cdot) = 1 - \sqrt{1 - \frac{8P_c^* n f_s L_{MT}}{V_{dc}V_j}} \tag{13}$$

Further, the phase shift between DC side bridges $\delta_{12}...\delta_{1j}...\delta_{1m}$ are calculated from the power flow requirement through the IMTx. The power from the AC side through the main transformers ($3r_jP_c$) is subtracted from the power requirement in the load port ($P_j$) to get the power through IMTx for the $j^{th}$ port. The relation between $\delta_{1j}$ and $P_{1j}$ as given in (9c) and other relations relating the power flow through the IMTx are inverted to calculate the phase shifts of DC side bridge as shown in Fig. 14. This relation is a coupled quadratic equation and will require a numerical solution if the number of load ports is more than two.

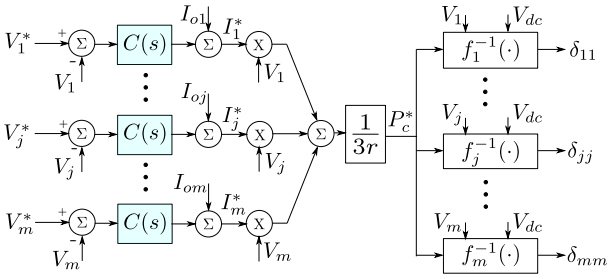

Fig. 13: Voltage controller and calculation of phase shifts.

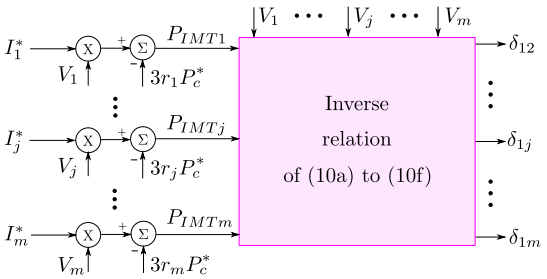


Fig. 14: Control block diagram for the power flow in IMTx.

## III. Design of the Converter

### A. *Preliminary Design*

The theoretical design of an MVAC to two port LVDC converter is discussed in this section for the specification given in Table. II. For medium voltage primary distribution level in India (11kV), peak phase voltage is 9kV ($11*\sqrt{2}/\sqrt{3}$). Going forward with 1700V SiC devices for the CHB bridge and AC side bridge, which can support 1200V DC bus, the required number of series connected modules per phase is calculated as 12 (9*1.1*1.1/(0.8*1.2)=11.34). This is under the following assumption: a) the maximum modulation index of the CHB bridge is 0.8, b) the maximum over voltage at the AC side is 10%, and c) the maximum drop across inductance is 10% in phase with converter voltage.

TABLE II: Specification for theoretical design

| Parameter | Symbol | Value |
|---|---|---|
| L-L MVAC voltage | $v_{gL-L}$ | 11 kV |
| Rated grid frequency | $f$ | 50 Hz |
| Number of ports | $m$ | 2 |
| Rated total power | $\Sigma P_i$ | 400 kW |
| Port 1 rated power | $P_{1r}$ | 200kW |
| Port 2 rated power | $P_{2r}$ | 200kW |
| Port 1 DC voltage | $V_1$ | 1000V |
| Port 2 DC voltage | $V_2$ | 1000V |
| Switching frequency | $f_s$ | 100 kHz |

With 12 modules connected per phase, the power flowing through the CHB bridge, AC side bridge and the main transformer is calculated as 11kW (400kW/(12*3)=11.11kW). The turns ratio of the main transformer is designed as $1:0.833$ to minimize the current stress [27]. Based on (5), to maintain the maximum phase shift ($\delta_{jj}$) less than 0.75, the main transformer series inductance is calculated as given in (14).

$$L_{MT} = \frac{V_{dc}V_j}{8nf_sP_c}\delta_{jj}(2-|\delta_{jj}|) = 150\mu H \tag{14}$$

### B. IMTx Design

Inter-module transformer (IMTx) is designed to handle the power transfer from one port to the other when two different ports are loaded differently. For a general case, when power in port 1 is $P_1$ and power in port 2 is $P_2$, the power coming from the AC side is $P_1+P_2$. The power processed by individual bridges in CHB, AC side bridge and the main transformer is calculated as given in (15). Half of the modules are combined to the DC side bridge connected to port 1, adding to a total power of $3rP_c/2$. With this, the power transferred through the IMTx is calculated as given in (16). The turns ratio for the IMTx is designed as $1:1$ to minimise the current stress for the given specification, [27].

$$P_c = \frac{1}{3r}(P_1+P_2) \tag{15}$$

$$P_{IMT} = \left(\frac{3r}{2}\right)P_c - P_1 = \frac{P_1+P_2}{2} - P_1 = \frac{P_2-P_1}{2} \tag{16}$$

With this, maximum power is transferred through IMTx when one port is generating maximum power ($P_1$=-200kW) and the other port is loaded at maximum power ($P_2$=200kW). Based on (6), to maintain the maximum phase shift ($\delta_{ij}$) less than 0.75, the IMTx series inductance is calculated as given in (17), (18). The peak and RMS current through the transformer is calculated as (19) and (20). The maximum flux linkage for the IMTx is calculated as given in (21).

$$L_{12} = \frac{V_1V_2}{8f_sP_{IMT}}\delta_{12}(2-|\delta_{12}|) = 5.86\mu H \tag{17}$$

$$L_1 = L_2 = L_{12}/2 = 2.93\mu H \tag{18}$$

$$i_{IMT,pk} = \frac{V_1}{4f_sL_{12}}\delta_{12} = 320A \tag{19}$$

$$i_{IMT,rms} = \frac{V_1\delta_{12}}{4f_sL_{12}}\sqrt{1-\frac{\delta_{12}}{3}} = 277A \tag{20}$$

$$n_1\Phi_{max} = \frac{V_1}{4f_s} = \frac{1000}{4*100*10^3} = 2.5\ mWbT \tag{21}$$

DC side bridge processes the power equal to the corresponding load port ($P_i$), and the voltage rating is the same as the load port voltage ($V_1 = V_2 = 1000V$). However, the current through the bridge is the combination of current through the main transformer and the IMTx. The wave shape and expression for RMS current change for different cases depending on the sign and magnitude of $\delta_{11}$ and $\delta_{12}$. $\delta_{11}$ and $\delta_{12}$ can be expressed as function power $P_1$ and $P_2$ as given in (22) and (23). Based on sign and magnitude of $\delta_{11}$ and $\delta_{12}$ the RMS value is evaluated in (24) to (29). From the equations, it can be derived that the maximum value of RMS current through the DC side bridge is when both ports are generating or consuming the rated load of $+/-200$ kW. This also concludes that the RMS current through the bridge or the semiconductor VA rating of the DC side bridge has remained the same compared to a single port ISOP solution with the same rating.

$$\delta_{11} = \text{sign}(P_c) * \left(1-\sqrt{1-\frac{8nf_sL_{MT}|P_c|}{V_{dc}V_1}}\right) \tag{22}$$

$$\delta_{12} = \text{sign}(P_{IMT}) * \left(1-\sqrt{1-\frac{8f_sL_{12}|P_{IMT}|}{V_2V_1}}\right) \tag{23}$$

$$\text{case I} \Rightarrow \delta_{11} > \delta_{12} > 0$$
$$i_{s1,rms} = \frac{V_1}{4f_sL_{12}}\sqrt{\begin{matrix}\delta_{11}^2+\delta_{12}^2+2\delta_{11}\delta_{12}-\delta_{12}^3 \\ -\delta_{11}^2\delta_{12}+\delta_{11}\delta_{12}^2-\delta_{11}^3/3\end{matrix}} \tag{24}$$

$$\text{case II} \Rightarrow \delta_{12} > \delta_{11} > 0$$
$$i_{s1,rms} = \frac{V_1}{4f_sL_{12}}\sqrt{\begin{matrix}-\delta_{11}^3+\delta_{11}^2\delta_{12}+\delta_{11}^2+\delta_{12}^2 \\ -\delta_{11}\delta_{12}^2+2\delta_{11}\delta_{12}-\delta_{12}^3/3\end{matrix}} \tag{25}$$

$$\text{case III} \Rightarrow \delta_{11} > 0,\ \delta_{12} < 0$$
$$i_{s1,rms} = \frac{V_1}{4f_sL_{12}}\sqrt{\begin{matrix}-\delta_{11}^3/3-\delta_{11}^2\delta_{12}+\delta_{11}^2+\delta_{12}^2 \\ +\delta_{11}\delta_{12}^2+2\delta_{11}\delta_{12}+\delta_{12}^3/3\end{matrix}} \tag{26}$$

$$\text{case IV} \Rightarrow \delta_{11} < 0,\ \delta_{12} > 0$$
$$i_{s1,rms} = \frac{V_1}{4f_sL_{12}}\sqrt{\begin{matrix}\delta_{11}^3/3+\delta_{11}^2\delta_{12}+\delta_{11}^2+\delta_{12}^2 \\ -\delta_{11}\delta_{12}^2+2\delta_{11}\delta_{12}-\delta_{12}^3/3\end{matrix}} \tag{27}$$

$$\text{case V} \Rightarrow \delta_{11} < \delta_{12} < 0$$
$$i_{s1,rms} = \frac{V_1}{4f_sL_{12}}\sqrt{\begin{matrix}2\delta_{11}\delta_{12}+\delta_{11}^2+\delta_{12}^2+\delta_{12}^3 \\ +\delta_{11}^3/3+\delta_{11}^2\delta_{12}-\delta_{11}\delta_{12}^2\end{matrix}} \tag{28}$$

$$\text{case VI} \Rightarrow \delta_{12} < \delta_{11} < 0$$
$$i_{s1,rms} = \frac{V_1}{4f_sL_{12}}\sqrt{\begin{matrix}\delta_{11}^3+2\delta_{11}\delta_{12}+\delta_{11}^2+\delta_{12}^2 \\ -\delta_{11}^2\delta_{12}+\delta_{12}^3/3+\delta_{11}\delta_{12}^2\end{matrix}} \tag{29}$$

### C. Controller Design

The plant mode is given in (30) based on Fig. 12. Considering the load feedforward, the plant model, along with the control architecture of the DC-DC stage, is shown in Fig. 13. From (30), it is observed that the voltage plant only depends on the output filter capacitor, and it is load-independent. For PV application, the DC port reference voltage $V_j^*$ is dictated by the maximum power point tracking (MPPT) algorithm, and in the case of battery load, it is dictated by the battery management system (BMS).

$$P(s) = \frac{V_j(s)}{I_j(s)-I_{oj}(s)} = \frac{1}{sC_j} * e^{-sT_d} \tag{30}$$

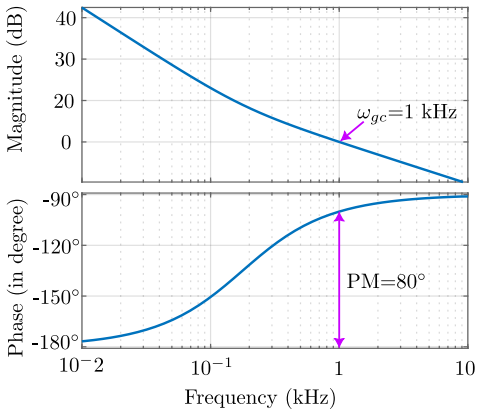


Fig. 15: Bode Plot of Loop Gain ($L_j$)

The control objective of the DC-DC stage include output voltage control of each port, and ensuring drawing of equal power from intermediate DC links. As the voltage loop of each port needs to track a DC reference voltage, a proportional-integral (PI) control is selected, leading to zero steady-state error. The loop gain for any $j^{th}$ port can be written as (31), here, $K_p$, and $K_i$ are the control parameters. The controller is designed to satisfy the following specifications, (a) zero steady-state error, (b) desired gain-cross over frequency ($\omega_{gc}$), (c) phase margin (PM) at the desired $\omega_{gc}$ should be at least $80^o$, in order to ensure the stability of the system. At a desired $w_{gc}$, the open-loop gain is represented in (32). The relationship with the desired PM with the $L_j$ at the desired $\omega_{gc}$ is given in (33). By solving the equations (32), and (33), the control parameters of $K_p$, and $K_i$ can be determined for the desired $\omega_{gc}$, and PM. Now, for the given $C_j = 10$ $\mu$F, $\omega_{gc} =$ 1 kHz, and PM=$80^o$, the designed parameters $K_p$, and $K_i$ are computed as 0.062, and 69.08, respectively. The bode-plot of the loop gain is shown, in Fig. 15.

$$L_j(s) = C_j(s)P(s) = \frac{K_p s + K_i}{s} \times \frac{1}{sC_j} \times e^{-sT_d} \tag{31}$$

$$|L_j(s)|_{s=j\omega_{gc}} = 1 \tag{32}$$

$$PM = -180 + \angle G_{OL}(s)_{s=j\omega_{gc}} \tag{33}$$

### D. *Effect of plant uncertainty*

For the model to be accurate, an exact plant model is required, and if there are uncertainties, it can lead to variation in transient response. The effect of uncertainty in the estimated series inductance is analyzed, where the actual value of series inductance ($L_{MT1}$, $L_{MT2}$ and $L'_{12}$) can vary from the estimated value ($L_{MT}$ and $L_{12}$). Through algebra, it can be shown that the uncertainty in series inductance will alter the gain ($P_c^*$ to $P_c$ and $P_{IMT}^*$ to $P_{IMT}$) from unity to the ratio of estimated inductance to the actual value. This modifies the control block diagram as shown in Fig. 16. It shows that the current to each port $I_1$ and $I_2$ has coupling from the other port directly related to uncertainty in series inductance. Per-unit uncertainty in series inductance $\Delta_{12}$, $\Delta_{MT1}$, and $\Delta_{MT2}$

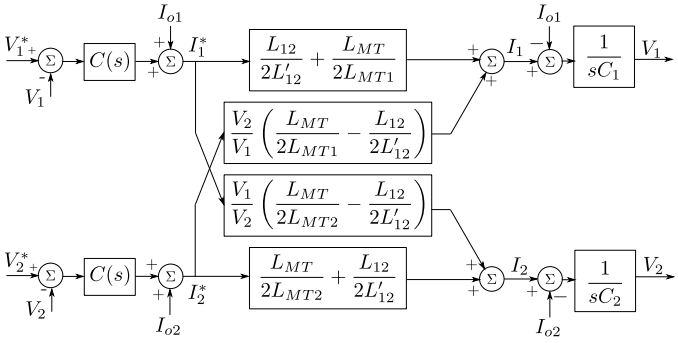


Fig. 16: Modified control block diagram incorporating plant uncertainties leading to coupling between output ports.

are introduced as defined in (34) to (36) to simplify the further calculation.

$$\Delta_{12} = (L_{12} - L'_{12})/L'_{12} \tag{34}$$

$$\Delta_{MT1} = (L_{MT} - L_{MT1})/L_{MT1} \tag{35}$$

$$\Delta_{MT2} = (L_{MT} - L_{MT2})/L_{MT2} \tag{36}$$

From the block diagram, the dynamic model of the converter output voltage can be expressed as given in (37). The plant uncertainty modifies the loop gain for the voltage controller; this affects the gain cross-over frequency and the phase margin but does not affect the steady-state performance. The controller can be designed to accommodate this variation in loop gain to have a sufficient phase margin for an expected worst-case variation in inductance. The load current and the current reference for the other port as a function of plant uncertainty as given in (37) also affects the output voltage.

$$\begin{aligned} V_1(s) = &\frac{\frac{C(s)}{sC_1}\left(1 + \frac{\Delta_{MT1} + \Delta_{12}}{2}\right)}{1 + \frac{C(s)}{sC_1}\left(1 + \frac{\Delta_{MT1} + \Delta_{12}}{2}\right)} \times V_1^*(s) \\ &+ \frac{\frac{1}{sC_1}\left(\frac{\Delta_{MT1} - \Delta_{12}}{2}\right)}{1 + \frac{C(s)}{sC_1}\left(1 + \frac{\Delta_{MT1} + \Delta_{12}}{2}\right)} \times I_2^*(s) \\ &+ \frac{\frac{1}{sC_1}\left(\frac{\Delta_{MT1} + \Delta_{12}}{2}\right)}{1 + \frac{C(s)}{sC_1}\left(1 + \frac{\Delta_{MT1} + \Delta_{12}}{2}\right)} \times I_{o1}(s) \end{aligned} \tag{37}$$

## IV. Results for a Scaled Prototype

### A. *Experimental set up*

A laboratory-scale MVAC to multi-port DC converter prototype is designed and developed with the parameters given in the table. III. A single-phase AC to two-port DC converter with two modules is developed as shown in Fig. 17, and the detailed schematic for it is shown in Fig. 18. SiC devices G3R40MT12K from GeneSic are used to realize the H-bridges, and gate driver ADuM4135 drives these devices from Analog devices. Texas Instruments microcontroller

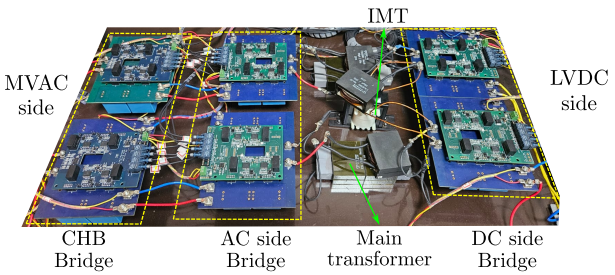


Fig. 17: SiC-based 1.2 kW hardware prototype with two ports.

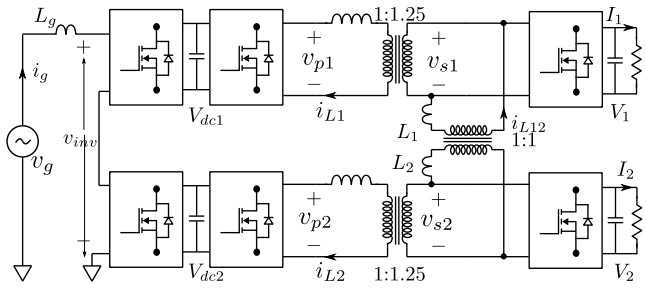


Fig. 18: Detailed schematic of the experimental set up.

TMS320F28379D is used for voltage and current sensing, closed-loop computation, and switching signal generation, with a clock frequency of 200MHz. The closed-loop computation time for the proposed solution with two ports is calculated as $14\mu s$ with this controller. A custom-designed planar transformer from Payton Planar is used to realize the main transformers. Tektronix scopes MSO46 and MDO 3104 are used to record the voltage and current waveform, and the power analyzer PW6001 from HIOKI is used to measure the efficiency and power factor.

TABLE III: Converter parameters for experimental verification

| Converter Parameter | Symbol | Value |
|---|---|---|
| MTx turns ratio | $1:n$ | 1:1.25 |
| IMTx turns ratio | – | 1:1 |
| Series Inductance of main transformers | $L_{MT}$ | 125 $\mu H$ |
| Series inductance of IMTx | $L_{12}$ | 105 $\mu H$ |
| Grid side filter | $L_g$ | 10 $mH$ |
| CHB DC bus capacitor | $C_{dc}$ | 2 $mF$ |
| Output filter Capacitor | $C_o$ | 10 $\mu F$ |

TABLE IV: Specification for experimental verification

| Parameter | Symbol | Value |
|---|---|---|
| Grid voltage | $v_g$ | 230 V |
| Number of ports | $m$ | 2 |
| Rated Power | $\Sigma P_i$ | 1.2 kW |
| Port 1 rated power | $P_1$ | 0.6 kW |
| Port 2 rated power | $P_2$ | 0.6 kW |
| Port 1 DC voltage | $V_1$ | 250 V |
| Port 2 DC voltage | $V_2$ | 250 V |
| Rated grid frequency | $f$ | 50 Hz |
| Switching frequency | $f_s$ | 50 kHz |

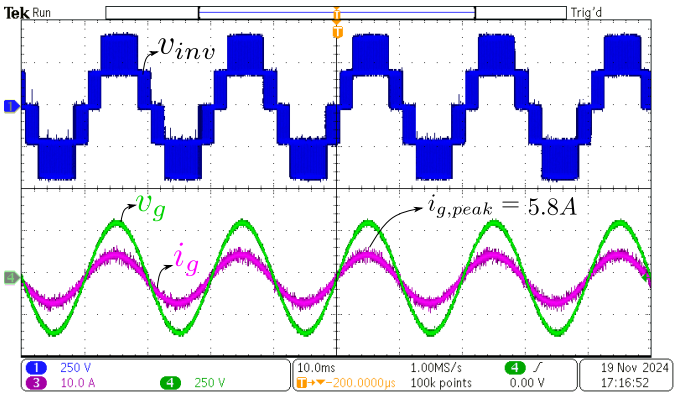


Fig. 19: Steady state performance of proposed IMT-based MVAC to multi-port LVDC solution indicating AC grid side voltage, $v_g$, inverter terminal voltage, $v_{inv}$, AC grid current, $i_g$ captured for five line cycles. [Ch.1: $v_{inv}$ 250 V/div., Ch.3: $i_g$ 10 A/div., Ch.4: $v_g$ 250 V/div., time scale: 10 ms/div.]

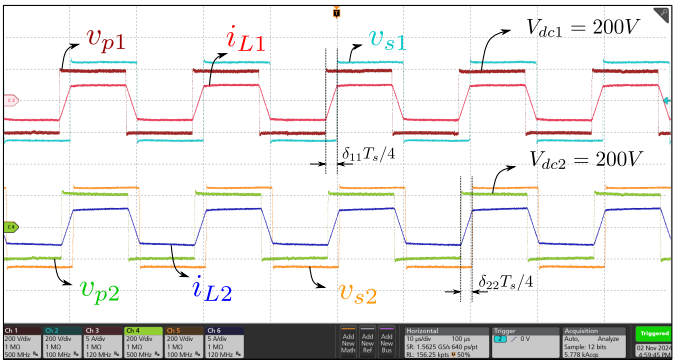


Fig. 20: High-frequency voltage and current waveform through MTx [Ch.1: $v_{p1}$ 200 V/div., Ch.2: $v_{s1}$ 200 V/div., Ch.3: $i_{L1}$ 5 A/div., Ch.4: $v_{p2}$ 220 V/div., Ch.5: $v_{s2}$ 200 V/div., Ch.6: $i_{L2}$ 5 A/div., time scale: 10 $\mu$s/div.].

### *B. Experimental Results*

The steady-state operation of the converter is verified with the specifications given in the table. IV. Steady state results for a loading of $P_1 = 300W$, and $P_2 = 600W$ is verified with a total of 0.9kW drawn from the AC grid. The AC side voltage and current waveform are given in Fig. 19. A sinusoidal current is drawn from the grid with a peak value of $5.8A$ at a power factor of 0.98. This closely matches the theoretical value of peak grid current ($5.5A = \sqrt{2} * 900/230$) at the unity power factor. The five-level inverter voltage generated at the inverter terminal after the grid side inductor filter ($L_g$) is also shown in the same figure. The AC-DC stage is switched at 10 kHz, and phase shift modulation is adopted for the CHB stage with two modules in series. The AC-DC stage also maintains the floating DC buses $V_{dc1} = V_{dc2} = 200V$ as seen from the amplitude of $V_{p1}$ and $V_{p2}$ in Fig. 20. The efficiency of the proposed solution is measured using the power analyzer for different output power, and is plotted in Fig. 21. The loss break down for a loading of 900W is shown in Fig. 22. The calculation for loss estimation is given below:

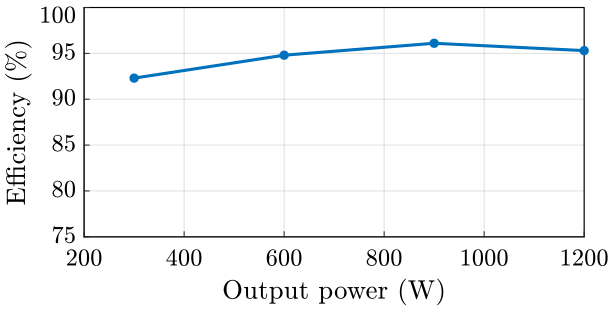


Fig. 21: Variation of estimated efficiency of the proposed solution for the variation in output power from 300W (25% of load) to 1200W (100% of load) at rated source and load voltage conditions.

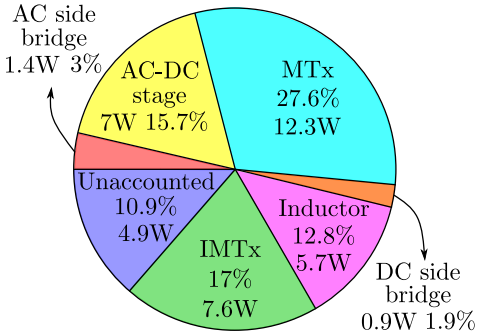


Fig. 22: Estimated loss breakdown within the system for a loading of $P_1 = 600W$, $P_2 = 300W$.

Conduction loss in CHB

$$8 * i_{CHB}^2 * R_{dson} = 8 * 2.76^2 * 0.05 = 3.36W \quad (38)$$

Conduction loss in MTx

$$2 * i_{\text{MT, rms}}^2 * R_{MTx} = 2 * 2.6^2 * 0.45 = 6.1W \quad (39)$$

Conduction loss in Inductor

$$2 * i_{\text{MT, rms}}^2 * R_L = 2 * 2.6^2 * 0.2 = 2.7W \quad (40)$$

Conduction loss in AC side Bridge

$$8 * i_{\text{ac side}}^2 * R_{dson} = 8 * 1.84^2 * 0.05 = 1.35W \quad (41)$$

Conduction loss in DC side Bridge

$$8 * i_{\text{dc side}}^2 * R_{dson} = 8 * 1.06^2 * 0.05 = 0.9W \quad (42)$$

Conduction loss in IMTx

$$i_{\text{IMT, rms}}^2 \times R_{IMTx} = 0.5^2 * 0.6 = 0.15W \quad (43)$$

The core loss for the main transformer is calculated as 6.25 W, the core loss for the inter-module transformer is calculated as 7.5 W, and the core loss for the inductor is calculated as 3 W. The switching loss for the CHb stage is calculated as 3.65 W. The difference between the estimated loss and measured loss is about 4.9 W, which is indicated as unaccounted in the loss breakdown chart.

The phase shift between the AC side bridge and the DC side bridge is decided to transfer an equal amount of power $P_c = (P_1 + P_2)/2 = 450W$. With a CHB DC bus voltage of $V_{dc1} = V_{dc2} = 200V$, output voltage of $V_1 = V_2 = 250V$, series inductance of main transformer $L_{MT}$, switching frequency of $f_s = 50kHz$ this phase shift is calculated from (5) as $\delta_{11} = \delta_{22} = 0.34$. Corresponding to this a phase shift of $\delta_{11}T_s/4 = 1.7\mu s$ is observed in Fig. 20. This phase shift $\delta_{11}$ between $v_{p1}$ and $v_{s1}$, and $\delta_{22}$ between $v_{p2}$ and $v_{s2}$ can be seen in Fig. 20 including the current through the main transformer. This demonstrates balanced power transfer through both main transformers, despite the difference in load requirements.

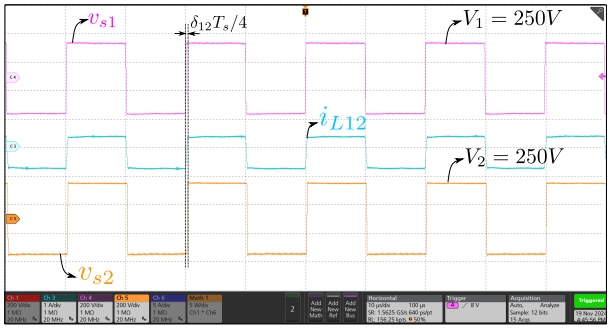


Fig. 23: High-frequency voltage and current waveform showing power transfer through IMTx [Ch.3: $i_{L12}$ 1 A/div., Ch.4: $v_{s1}$ 220 V/div., Ch.5: $v_{s2}$ 200 V/div., time scale: 10 $\mu$s/div.].

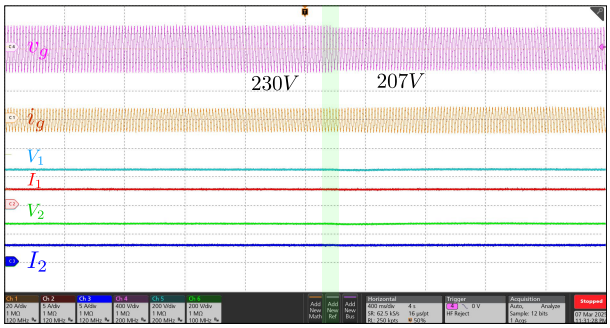


Fig. 24: Performance during voltage sag condition in grid voltage, $v_g$ for a 10% reduction from rated 230 V to 207 V, indicating the AC side grid voltage waveforms, $v_g$, AC side grid current waveforms, $i_g$, Port 1 & 2 DC output voltage and current waveforms ($V_1$, $I_1$) & ($V_2$, $I_2$) respectively. [Ch.1: $i_g$ 20 A/div., Ch.2: $I_1$ 5 A/div., Ch.3: $I_2$ 5 A/div., Ch.4: $v_g$ 400V/div., Ch. 5: $V_1$ 200V/div., Ch. 6: $V_2$ 200V/div, time scale: 400ms/div.]

The difference in power between the load port and the power through the main transformer, $P_{IMTx} = (P_2 - P_1)/2 = 150W$, is transferred through the inter-module transformer with a phase shift between $v_{s1}$ and $v_{s2}$. This phase shift is calculated based on (6) as $\delta_{12} = 0.05$ and the corresponding time delay between $v_{s1}$ and $v_{s2}$ is shown in Fig. 23 as $0.26\mu s$. The figure also shows the current through the IMT as $i_{L12}$. These steady-state results also show that the output voltage, $V_1$ and $V_2$, are maintained at the reference value $250V$.

Transient response for a step change in grid voltage and frequency are observed to validate the system's robustness. Step changes in AC side voltage is introduced using programmable AC power source 61704 from Chroma. Voltage sag is emulated

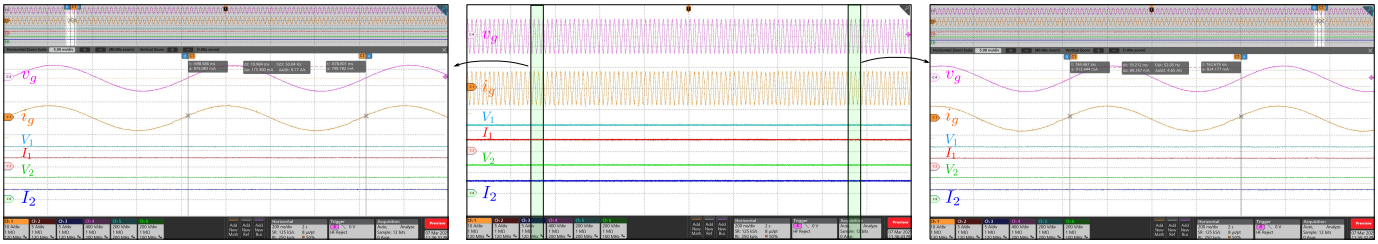


Fig. 25: Input and output voltage and currents for a change in grid frequency from 50Hz to 52Hz at $P_1 = 600W$, $P_2 = 600W$. [Ch.1: $i_g$ 10 A/div., Ch.2: $I_1$ 5 A/div., Ch.3: $I_2$ 5 A/div., Ch.4: $v_g$ 400 V/div., Ch. 5: $V_1$ 200 V/div., Ch. 6: $V_2$ 200 V/div, time scale: 20 ms/div.]

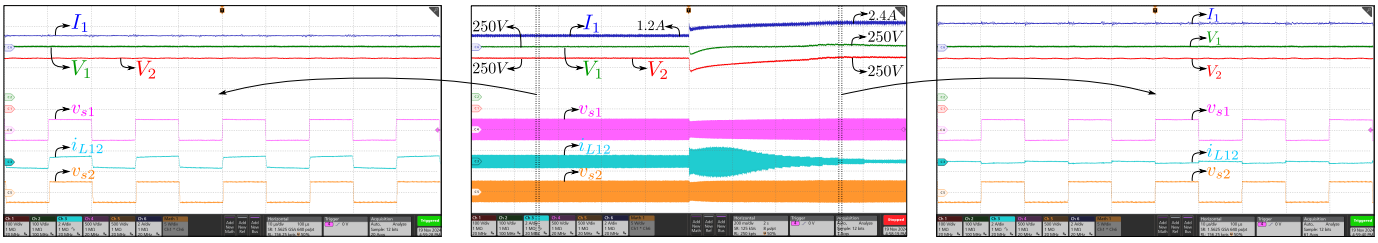


Fig. 26: DC side voltages, current and high-frequency voltage and current through the inter module transformer for a step change in $P_2$ from 300W to 600W while $P_1$ = 600W. The waveform is zoomed over a few switching cycle before and after the transient to show the different in power through the inter module transformer.

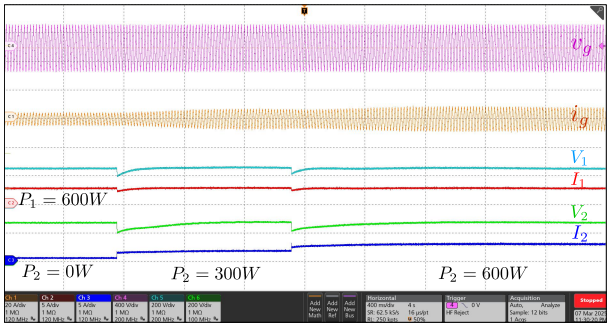


Fig. 27: Input and output voltages and currents for a step change in port 2 power from 0W to 600W while $P_1 = 600W$. [Ch.1: $i_g$ 20 A/div., Ch.2: $I_1$ 5 A/div., Ch.3: $I_2$ 5 A/div., Ch.4: $v_g$ 400 V/div., Ch. 5: $V_1$ 200 V/div., Ch. 6: $V_2$ 200 V/div, time scale: 20 ms/div.]

by giving a 10% reduction in AC side voltage from 230 V to 207 V as shown in Fig. 24. Both the DC port voltages are regulated to the required 250V at 600W power each during this transient verifying the systems robustness. System response for a step change in AC side frequency is observed using the same programmable AC power source. The transient response is shown in Fig. 25 for a step change in frequency from 50Hz to 52Hz. The system is able to track the DC side voltage for this variation of grid frequency verifying its robustness to frequency variation.

The dynamic performance of the converter is verified by switching the load in port 1 from $300W$ to $600W$ while port 2 is continuously loaded at $P_2 = 600W$. Fig. 26 shows the voltage and current waveform during this transient. The closed loop controller corrects the output voltage to $250V$ for this step change in load in port 1. The voltage and current through the IMT before and after the transient is also shown in the same figure. This waveform over a few switching cycles shows the change in power through IMT from 150W to 0W. The transient response for a step change in load in one of the ports is also shown along with AC side and DC side voltage and current waveform in Fig. 27.

Experiment is also carried out for a case where one of the DC ports is supplying power to the system, and the other DC port is loaded. Port 2 is supplying a power of $P_2 = -600W$ to the system and port 1 is loaded at $P_1 = 300W$. The remaining power of 300W is supplied to the AC side. The steady-state result with AC side voltage, current, DC side voltages and current for this case is shown in Fig. 28. Additionally, the high-frequency voltage and current waveform of the main transformer are given in Fig. 29. The AC side bridge lags the DC side side bridge to transfer a power of 150W through each of the main transformers.

## V. Conclusion

This paper presents a novel medium voltage AC to isolated multi-port DC converter tailored for the increasing power demands of electric vehicle fast-charging stations. The proposed solution addresses critical inefficiencies in existing line frequency transformer-less solutions. It eliminates intermediate energy storage and additional MV-insulated transformer windings required for power balancing in input series output parallel (ISOP) based converters. The proposed solution also maintains the same semiconductor VA rating of ISOP-based two-stage MVAC to single-port LVDC converter, unlike the solutions in the literature that need additional devices to maintain power balance. The modular design with bidirectional power flow capability enables seamless integration of local energy storage and renewable energy sources, reducing

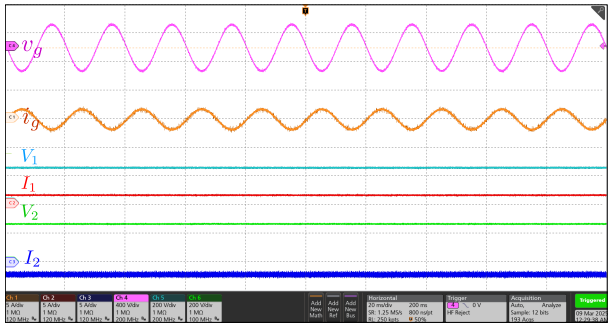


Fig. 28: Steady state performance with port 1 operating at 300W and port 2 operating at -600W, indicating the AC side grid voltage waveforms, $v_g$, AC side grid current waveforms, $ig$, Port 1 & 2 DC output voltage and current waveforms ($V_1$, $I_1$) & ($V_2$, $I_2$) respectively. [Ch.1: $i_g$ 5 A/div., Ch.2: $I_1$ 5 A/div., Ch.3: $I_2$ 5 A/div., Ch.4: $v_g$ 400 V/div., Ch. 5: $V_1$ 200 V/div., Ch. 6: $V_2$ 200 V/div, time scale: 20 ms/div.]

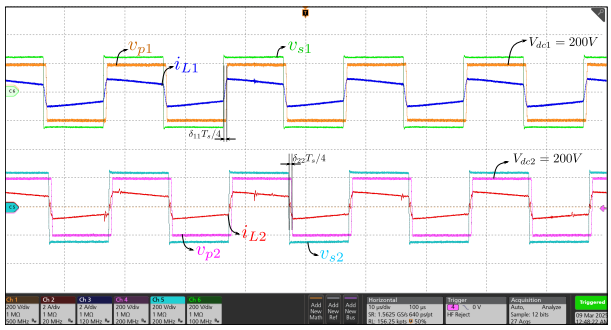


Fig. 29: Steady state performance of the proposed solution with port 1 operating at 300W and port 2 operating at -600W, indicating main transformers' waveforms at both ports, namely Port 1 primary side transformer voltage $v_{p1}$, Port 1 primary side transformer current $i_{L1}$, Port 1 secondary side transformer voltage $v_{s1}$, Port 2 primary side transformer voltage $v_{p2}$, Port 2 primary side transformer current $i_{L2}$, Port 2 secondary side transformer voltage $v_{s2}$ respectively. [Ch.1: $v_{p1}$ 200 V/div., Ch.2: $i_{L2}$ 2 A/div., Ch.3: $i_{L1}$ 2 A/div., Ch.4: $v_{p2}$ 200 V/div., Ch. 5: $v_{s2}$ 200 V/div., Ch. 6: $v_{s1}$ 200 V/div, time scale: 10us/div.]

grid dependency and enhancing the operational stability of futuristic fast charging stations. The proposed system supports independent control of each LVDC port while drawing high-quality UPF current from the MVAC grid.

A systematic design methodology for an MVAC to two port LVDC configuration has been presented, and the concept has been validated experimentally using a scaled prototype. The experimental results confirm the effectiveness of the proposed design, demonstrating high efficiency (95.3%), independent power flow capabilities, and robust voltage regulation under varying load conditions. These features make the proposed converter a promising solution for future electric vehicle fast-charging infrastructure, combining scalability, energy efficiency, and adaptability to renewable energy integration.

## REFERENCES

[1] H. P V, S. Kasicheyanula, S. Mathapati, and K. Basu, "A Three-phase MVAC to Multi-port LVDC Converter with High Frequency Isolation for Fast DC Charging Station for EVs," in *2023 IEEE Energy Conversion Congress and Exposition (ECCE)*, 2023, pp. 33–38.

[2] G. Arena, A. Chub, M. Lukianov, R. Strzelecki, D. Vinnikov, and G. De Carne, "A Comprehensive Review on DC Fast Charging Stations for Electric Vehicles: Standards, Power Conversion Technologies, Architectures, Energy Management, and Cybersecurity," *IEEE Open Journal of Power Electronics*, vol. 5, pp. 1573–1611, 2024.

[3] S. S. G. Acharige, M. E. Haque, M. T. Arif, N. Hosseinzadeh, K. N. Hasan, and A. M. T. Oo, "Review of Electric Vehicle Charging Technologies, Standards, Architectures, and Converter Configurations," *IEEE Access*, vol. 11, pp. 41 218–41 255, 2023.

[4] H. Tu, H. Feng, S. Srdic, and S. Lukic, "Extreme Fast Charging of Electric Vehicles: A Technology Overview," *IEEE Transactions on Transportation Electrification*, vol. 5, no. 4, pp. 861–878, 2019.

[5] P. V. Harisyam, D. Das, and K. Basu, "An Efficient and Compact Single-Stage High-Frequency-Link Medium Voltage AC to DC Converter," in *2021 IEEE Energy Conversion Congress and Exposition (ECCE)*, 2021, pp. 532–537.

[6] S. Mazumder, A. Pal, and K. Basu, "A Single-Stage Soft-Switched LVDC to Three-Phase MVAC Converter for MV Grid Integration of Utility-Scale Solar PV," in *2023 11th International Conference on Power Electronics and ECCE Asia (ICPE 2023 - ECCE Asia)*, 2023, pp. 1504–1508.

[7] W. Xu, Z. Guo, A. Vetrivelan, R. Yu, and A. Q. Huang, "Hardware Design of a 13.8-kV/3-MVA PV Plus Storage Solid-State Transformer (PVS-SST)," *IEEE Journal of Emerging and Selected Topics in Power Electronics*, vol. 10, no. 4, pp. 3571–3586, 2022.

[8] D. Dong, M. Agamy, J. Z. Bebic, Q. Chen, and G. Mandrusiak, "A Modular SiC High-Frequency Solid-State Transformer for Medium-Voltage Applications: Design, Implementation, and Testing," *IEEE Journal of Emerging and Selected Topics in Power Electronics*, vol. 7, no. 2, pp. 768–778, 2019.

[9] H. P V and K. Basu, "A Single-Stage High-Frequency-Link Medium Voltage AC to DC Converter for Utility-Scale Grid Integration of Solar and Storage," *IEEE Transactions on Power Electronics*, pp. 1–14, 2024.

[10] A. Blinov, A. Chub, N. Guler, S. Bayhan, L. Parsa, and D. Vinnikov, "Modular mv naturally balanced converter with high-frequency isolation and no dc-link capacitor for ev fast charging," *IEEE Transactions on Transportation Electrification*, vol. 11, no. 1, pp. 1141–1150, 2025.

[11] S. Srdic and S. Lukic, "Toward Extreme Fast Charging: Challenges and Opportunities in Directly Connecting to Medium-Voltage Line," *IEEE Electrification Magazine*, vol. 7, no. 1, pp. 22–31, 2019.

[12] S. Valedsaravi, A. El Aroudi, and L. Martínez-Salamero, "Review of Solid-State Transformer Applications on Electric Vehicle DC Ultra-Fast Charging Station," *Energies*, vol. 15, no. 15, 2022. [Online]. Available: https://www.mdpi.com/1996-1073/15/15/5602

[13] A. Ahmad, Z. Qin, T. Wijekoon, and P. Bauer, "An Overview on Medium Voltage Grid Integration of Ultra-Fast Charging Stations: Current Status and Future Trends," *IEEE Open Journal of the Industrial Electronics Society*, vol. 3, pp. 420–447, 2022.

[14] J. T. Hawke, H. S. Krishnamoorthy, and P. N. Enjeti, "A Family of New Multiport Power-Sharing Converter Topologies for Large Grid-Connected Fuel Cells," *IEEE Journal of Emerging and Selected Topics in Power Electronics*, vol. 2, no. 4, pp. 962–971, 2014.

[15] A. Karbozov, M. G. Majumder, H. S. Krishnamoorthy, and K. Rajashekara, "Triple Active Bridge Based Multiport Energy Router for Subsea – Renewable Interconnection," *IEEE Transactions on Industry Applications*, vol. 59, no. 4, pp. 4528–4538, 2023.

[16] Y. Zhuang, F. Liu, Y. Huang, S. Wang, S. Pan, X. Zha, and X. Diao, "A Multiport DC Solid-State Transformer for MVDC Integration Interface of Multiple Distributed Energy Sources and DC Loads in Distribution Network," *IEEE Transactions on Power Electronics*, vol. 37, no. 2, pp. 2283–2296, 2022.

[17] Y. Zhuang, F. Liu, Y. Huang, Z. Liu, S. Pan, X. Zha, and J. Jiang, "A Multiport Modular DC–DC Converter With Low-Loss Series LC Power Balancing Unit for MVDC Interface of Distributed Photovoltaics," *IEEE Transactions on Power Electronics*, vol. 36, no. 7, pp. 7736–7749, 2021.

[18] S. Zhao, Y. Chen, S. Cui, B. J. Mortimer, and R. W. De Doncker, "Three-Port Bidirectional Operation Scheme of Modular-Multilevel DC–DC Converters Interconnecting MVDC and LVDC Grids," *IEEE Transactions on Power Electronics*, vol. 36, no. 7, pp. 7342–7348, 2021.

[19] A. Marzoughi, R. Burgos, D. Boroyevich, and Y. Xue, "Design and Comparison of Cascaded H-Bridge, Modular Multilevel Converter, and 5-L Active Neutral Point Clamped Topologies for Motor Drive Applications," *IEEE Transactions on Industry Applications*, vol. 54, no. 2, pp. 1404–1413, 2018.
[20] M. Vasiladiotis and A. Rufer, "A Modular Multiport Power Electronic Transformer With Integrated Split Battery Energy Storage for Versatile Ultrafast EV Charging Stations," *IEEE Transactions on Industrial Electronics*, vol. 62, no. 5, pp. 3213–3222, 2015.
[21] K. H.-s. R. M.-h. K. M.-h. Baek Joo-won, Kim Myeong-ho, "Power converter," May 7 2019, wIPO (PCT) WO 2020/091168 A1. [Online]. Available: https://patents.google.com/patent/WO2020091168A1/en?oq=WO+2020%2f091168+A1
[22] C. L. L. H. Kong, "Power conversion system and control method," Nov. 7 2022, uS 2022/0158549 A1. [Online]. Available: https://patents.google.com/patent/US20220158549A1/en?oq=US+2022%2f0158549+A1
[23] Y. Ko, M. Andresen, G. Buticchi, and M. Liserre, "Power Routing for Cascaded H-Bridge Converters," *IEEE Transactions on Power Electronics*, vol. 32, no. 12, pp. 9435–9446, 2017.
[24] J. Liu, J. Yang, J. Zhang, Z. Nan, and Q. Zheng, "Voltage Balance Control Based on Dual Active Bridge DC/DC Converters in a Power Electronic Traction Transformer," *IEEE Transactions on Power Electronics*, vol. 33, no. 2, pp. 1696–1714, 2018.
[25] K. Zhang, Z. Shan, and J. Jatskevich, "Large- and Small-Signal Average-Value Modeling of Dual-Active-Bridge DC–DC Converter Considering Power Losses," *IEEE Transactions on Power Electronics*, vol. 32, no. 3, pp. 1964–1974, 2017.
[26] S. Madineni, P. V. Harisyam, D. Das, S. Paul, U. Kundu, P. Dey, S. Ghotgalkar, and K. Basu, "Dynamic Modeling and Control of Dual-Active- Bridge DC–DC Converter With Triple-Phase-Shift Modulation," *IEEE Power Electronics Magazine*, vol. 11, no. 4, pp. 45–53, 2024.
[27] D. Das and K. Basu, "Optimal Design of a Dual-Active-Bridge DC–DC Converter," *IEEE Transactions on Industrial Electronics*, vol. 68, no. 12, pp. 12 034–12 045, 2021.

**Harisyam P V** (Student Member, IEEE) received the B.Tech. degree in Electrical and Electronics Engineering from the National Institute of Technology, Calicut, India, in 2018, the M.Tech. degree from the Indian Institute of Science, Bengaluru, India, in 2020, in electrical engineering sponsored by Texas Instruments India. He is currently pursuing the Ph.D. degree at the Electrical Engineering Department, IISc, Bangalore, India. His research interests include topology modulation and control of medium voltage power electronic converters.

**K. Saichand** (S'12) received his M.E. and Ph.D. degrees from the Department of Electrical Engineering, Indian Institute of Science (IISc) Bangalore, India in 2012 and 2018 respectively. He is currently working as an Electrical design principal engineer in Delta Electronics India Pvt. Ltd. His current research interests are super-capacitors and advanced energy storage, DC/DC converters, AC/DC converters, SST technologies, high power converters, medium voltage power conversion.

**Surjakanta Mazumder** (Student Member, IEEE) holds a B.Tech. in Electrical Engineering from Maulana Abul Kalam University of Technology, Kolkata (2018), and an M.Tech. in Power Electronics from SVNIT Surat (2021). He worked as a Project Associate at IISc Bangalore (2021–2022), contributing to power electronic converters for space applications under the ISRO-IISc Mission Mode Project. Since 2022, he is pursuing PhD in Power Electronics at IISc, focusing on high-frequency linked converters for medium voltage transformers and EV charging.

**Shashidhar Mathapati,** CTO of Delta Electronics India, is an expert in power electronics and advanced motor drives with over two decades of experience. He holds a doctorate (Dr.-Ing.) from the University of Paderborn, Germany. He started his carrier in Delta with an ambitious high-power R&D team known as MWP (Mega Watt Power). Since his tenure in MWP, been focused majorly on high-power, medium and low voltage efficient power conversion technology and advanced motor drives. From 2019 onward he is heading the complete R&D operations of Delta India Electronics.

**Kaushik Basu** (Senior Member, IEEE) received Ph.D. degree in electrical engineering from the University of Minnesota, Minneapolis, in 2012. He was a Design Engineer with Cold Watt India in 2006 and an Electronics and Control Engineer with Dynapower Corporation USA from 2013-2015. He is currently an Associate Professor with the Department of Electrical Engineering, Indian Institute of Science. He has been an author and co-author of several technical papers published in peer-reviewed journals and conferences. His research interests include various aspects of the general area of Power Electronics. He is the founding chair of both IEEE PELS and IES Bangalore Chapter.